Research Square

Preprints are preliminary reports that have not undergone peer review.
They should not be considered conclusive, used to inform clinical practice,
or referenced by the media as validated information.

PPP2CA Drives Chondrocyte Metabolic Disorders and Underpins Osteoarthritis Pathogenesis through Targeting AMPK Dephosphorylation

Ke Lu

luke35238330126.com

Shenzhen Hospital, Southern Medical University https://orcid.org/0000-0002-1641-4748

Jingwen Li

Center for AI-Driven Medical Research, Shenzhen Institutes of Advanced Technology, Chinese Academy of Sciences, Shenzhen 518055, China

Yu-Ching Hsu

Department of Orthopedics, Shenzhen Hospital, Southern Medical University, Shenzhen 518101, China

Guizheng Wei

Department of Bone and Joint Surgery, the First Affiliated Hospital of Guangxi Medical University https://orcid.org/0009-0006-0479-5076

Zewei Li

Department of Orthopedics, Shenzhen Hospital, Southern Medical University, Shenzhen 518101, China

Rui Du

State Key Laboratory of Pharmaceutical Biotechnology, Division of Sports Medicine and Adult Reconstructive Surgery, Department of Orthopedic Surgery, Nanjing Drum Tower Hospital, Affiliated Hospital

Qing Jiang

Drum Tower Hospital affiliated to Medical School of Nanjing University https://orcid.org/0000-0002-2552-9686

Hongxun Sang

Shenzhen Hospital, Southern Medical University

Bin Xue

Nanjing medical University https://orcid.org/0000-0002-2713-2156

Hong Pan

Guangdong Key Laboratory of Nanomedicine, CAS-HK Joint Lab of Biomaterials, CAS Key Laboratory of Biomedical Imaging Science and System, Shenzhen Institute of Advanced Technology, Chinese Academy of

Di Chen

Shenzhen Institute of Advanced Technology, Chinese Academy of Sciences https://orcid.org/0000-0002-4258-3457

Lizhen Zhu

Guangdong Key Laboratory of Nanomedicine, CAS-HK Joint Lab of Biomaterials, CAS Key Laboratory of Biomedical Imaging Science and System, Shenzhen Institute of Advanced Technology, Chinese Academy of

---

Article

Keywords: PPP2CA, chondrocyte, AMPK signaling, osteoarthritis, mitochondrial dysfunction

Posted Date: April 16th, 2026

DOI: https://doi.org/10.21203/rs.3.rs-9176742/v1

License: This work is licensed under a Creative Commons Attribution 4.0 International License. Read Full License

Additional Declarations: There is no conflict of interest

Abstract

Osteoarthritis (OA) is a debilitating degenerative joint disease with limited therapeutic options. Emerging evidence implicates that metabolic disorder is the major risk factor in OA pathogenesis, with dysfunction in AMP-activated protein kinase (AMPK) signaling. AMPK is a central metabolic sensor and is activated by phosphorylation and inactivated by dephosphorylation. Dysruption of the steady-state protein levels of AMPK affects energy balance and promotes inflammation, mitochondrial dysfunction, and catabolic activation in chondrocytes. While metformin, an AMPK activator, has shown clinical promising in alleviating OA symptoms, its limited efficacy highlights the need for alternative strategies targeting AMPK regulatory mechanisms. Protein phosphatase 2A (PP2A), particularly its catalytic subunit alpha (PPP2CA), is a major serine/threonine phosphatase responsible for AMPK dephosphorylation. Here, we identified PPP2CA as a central regulator of metabolic homeostasis in OA pathogenesis. Chondrocyte-specific deletion of *Ppp2ca* restored AMPK signaling, preserved mitochondrial integrity, as evidenced by reduced ROS, enhanced ATP production and suppressed catabolic gene expression, resulting in attenuation of OA progression in mice. We further assessed the therapeutic potential of targeting AMPK dephosphorylation using a PPP2CA inhibitor LB-100 for OA treatment. We engineered yeast-microcapsule microrobots encapsulating LB-100 (YC-LB-100), enabling oral delivery and macrophage-mediated targeting to inflamed joints. YC-LB-100 reversed pain behaviors and reduced cartilage erosion in a DMM-induced OA mouse model. Our findings reveal that PPP2CA is a critical enzyme mediating AMPK dephosphorylation and regulating AMPK activity in chondrocytes, positioning PPP2CA as a novel therapeutic target for OA management.

Introduction

Osteoarthritis (OA) is a global condition affecting millions, resulting in substantial financial and medical burdens for both patients and healthcare systems[1]. Despite its widespread impact, there are currently no effective biomarkers or disease-modifying therapeutics available for early detection and management of the disease[2]. Although the exact cause of OA remains unclear, a growing body of evidence indicates that energy metabolism plays a pivotal role in maintaining cartilage function, and its dysregulation leads to the initiation and progression of OA[3,4]. Within this context, the AMPK stands out as a central signaling hub that integrates metabolic stress signals to preserve cartilage homeostasis.

AMPK orchestrates metabolic reprogramming through multiple pathways: it enhances glucose uptake via GLUT1/4, promotes fatty acid oxidation through PPARα activation, suppresses anabolic mTOR signaling, and coordinates with HIF-1α to regulate mitochondrial homeostasis and ROS production[5–10]. Critically, AMPK undergoes pathological dephosphorylation at Thr172 in both human OA chondrocytes and experimental OA animal models[11]. Inhibition of AMPK activity by dephosphorylation disrupts chondrocyte homeostasis through different mechanisms: for example, impairing autophagy which leads to mitochondrial dysfunction and oxidative stress[12,13]; shifting oxidative phosphorylation to glycolysis, and enhancing the inflammatory response and expression of catabolic genes[14,15]. Collectively, these

defects establish AMPK dephosphorylation as a key event in OA progression. Accordingly, pharmacological activation of AMPK has emerged as a therapeutic strategy and the AMPK activator, metformin, has been demonstrated to have chondroprotective effects in preclinical studies and recent clinical data showed that metformin improved knee function and alleviated knee pain in overweight OA patients[16]. However, due to the limited efficacy of metformin, alternative approaches need to be developed. Rather than activation of AMPK phosphorylation, targeting the phosphatases responsible for AMPK dephosphorylation may offer a more specific and complementary therapeutic strategy.

PP2A, belongs to the family of serine/threonine phosphatases, targets more than 300 phosphoproteins that govern cell-cycle progression, metabolism, transcription, apoptosis, and cytoskeletal dynamics[19]. Due to its ability to form diverse oligomeric complexes, PP2A emerges as the central gatekeeper of the phosphorylation/dephosphorylation equilibrium[20–22]. For this reason, PP2A intersects with many proteins involving in almost every major signaling pathways, making it an indispensable regulator of cellular phospho-proteostasis[23]. PP2A catalytic subunit alpha (PP2Aca, encoded by *PPP2CA*) is the key functional subunit of PP2A. Studies indicate that global knockout of *Ppp2ca* in mice results in embryonic lethality due to impaired mesoderm induction, establishing that this subunit is essential for cell survival in the fetal state[24]. Several recent studies demonstrate that PPP2CA in different tissues and organs in the body. However, the regulatory function of PPP2CA-mediated protein dephosphorylation in cartilage homeostasis remains poorly understood.

In the present studies, we generated chondrocyte-specific *Ppp2ca* ablation animal model to delineate its functional impact on OA progression and uncover underlying molecular mechanisms. This study was designed to decipher functions of PPP2CA in cartilage homeostasis and understand which phosphorylation-dependent metabolic networks contribute to OA pathogenesis. Finally, as a translational approach based on mechanistic studies, we assess the therapeutic potential of the PPP2CA inhibitor, LB-100, in OA treatment.

Results

Multi-omics profiling identifies PPP2CA-mediated metabolic dysfunction in OA

From the perspective of phosphorylation-dephosphorylation equilibrium, we utilized phosphoproteomics analysis to systematically characterize changes in protein phosphorylation during OA progression. Analysis of OA patient specimens demonstrated a phosphorylation profile with 17 distinct phosphorylation alterations relative to healthy controls (Fig. 1a). In healthy donors, we identified two protein phosphorylation events related to HIF-1α signaling and one associated with ATP binding, suggesting AMPK activation in this population. In contrast, no AMPK-related signaling was detected in OA patient specimens, indicating AMPK inactivation during OA progression. Hence, these findings implicate protein dephosphorylation in AMPK during OA development, prompting us to investigate the

role of the major AMPK phosphatase, PP2A. To elucidate the expression profile of its catalytic subunit PPP2CA in cartilage, we first interrogated *PPP2CA* expression patterns in publicly available OA transcriptome database (MSdb)[28]. Bioinformatic analysis revealed that PPP2CA expression levels (measured in Reads Per Kilobase per Million mapped reads, RPKM) were significantly increased in OA cartilage (Fig. 1b). This finding was validated at the protein level by immunohistochemical (IHC) analysis, showing pronounced PPP2CA accumulation in lesioned region of articular cartilage in OA patients (Fig. 1c,d). We next established a destabilization of medial meniscus (DMM)-induced murine OA model to further determine *PPP2CA* expression in OA anamial models. Immunofluorescence (IF) analysis of the mice with 8 weeks post DMM surgery revealed a 2-fold upregulation of PPP2CA expression (Fig. 1e,f). Consistent with the *in vivo* findings, *in vitro* study also showed 2.5-fold *PPP2CA* upregulation after IL-1β (10 ng/mL, 24h) stimulation in ATDC5 chondrogenic cells (Fig. 1g,h).

Genetic ablation of PPP2CA in chondrocytes attenuates OA pathogenesis

To investigate the impact of PPP2CA in chondrocytes during OA pathogenesis, we generated chondrocyte-specific *PPP2CA* conditional knockout (cKO) mice by breeding *Ppp2ca*$^{flox/flox}$ mice with *Col2-CreER* transgenic mice (Fig. S1a,b). We also bred *Col2-CreER* mice with ZsGreen-tdTomato reporter mice and analyzed reporter activity showing effective localization of reporter activity in acticular chondrocytes (Fig. S1c).

Next, to determine whether *Ppp2ca* cKO alleviates OA-related pain, we established OA models by performing DMM surgery on 10-week-old *Ppp2ca* cKO mice and their Cre-negative littermate control. Both mice were assessed using von Frey test (testing the mechanical allodynia) DMM-induced OA mice exhibited reduction of withdraw thresholds (indicating increased pain sensitivity), which were reversed by *Ppp2ca* cKO (Fig. 2a). Pain-related spontaneous activities were analyzed by LABORAS™ system, revealing significantly increased movement trajectories in *Ppp2ca* cKO mice compared to the Cre-negative control mice received DMM surgery at the same time (Fig. 2b). *Ppp2ca* cKO mice showed elevated average speed (Fig. 2c), distance (Fig. 2d), locomotion frequency (Fig. 2e), rear frequency (Fig. 2f), and climb frequency (Fig. 2g). Micro-CT analysis showed pronounced osteophyte formation in Cre-negative control mice after DMM surgery; whereas *Ppp2ca* cKO mice exhibited reduced subchondral bone volume (Fig. 2h,i) and osteophyte maturity (Fig. 2h,j). To evaluate cartilage degradation, Safranin O/Fast green-stained sections were scored using the OARSI scoring system (a semi-quantitative measure of OA). DMM-induced cartilage destructions were significantly attenuated in *Ppp2ca* cKO, demonstrated by reduced OARSI scores by approximately 62% compared to Cre-negative control mice 16-weeks after DMM surgery (Fig. 2k,l). Histological analysis indicated partial restoration of cartilage area in KO mice (Fig. 2m). Synovial inflammation and osteophyte formation, evident by synovitis scores and osteophyte size and maturity 16-weeks after DMM surgery (Fig. S2a-c), were markedly suppressed in *Ppp2ca* cKO mice. IHC analysis revealed that *Ppp2ca* cKO suppressed expression of catabolic markers ADAMTS5 (Fig. 2n,o), MMP13 (Fig. S2d,e), and CCL2 (Fig. 2d,f), while enhancing Aggrecan (ACAN)-positive cartilage area (Fig. 2n,p). Bone microarchitecture analysis demonstrated no significant differences in trabecular bone mineral density (BMD) (Fig. S2i), trabecular number (Fig. S2j), trabecular

thickness (Fig. S2k), trabecular separation (Fig. S2l), or cortical bone thickness (Fig. S2m) between the two strains of mice.

To further investigate the role of PPP2CA in OA progression, we generated *Ppp2ca*-knockdown in ATDC5 chondrocyte-like cell lines using lentiviral vectors. qPCR analysis revealed that mRNA levels of cartilage extracellular matrix (ECM)-degrading genes (*Mmp3, Mmp13, Adamts4, Adamts5*) were significantly reduced in *Ppp2ca*-knockdown cells following IL-1β-induced injury (Fig. S3a-d). Conversely, mRNA levels of ECM synthesis-related genes (*Col2a1, Acan*) were upregulated in *Ppp2ca* knockdown cells compared to controls after IL-1β stimulation (Fig. S3e,f).

Ppp2ca deficiency activates AMPK signalling and its downstream target genes

To elucidate the molecular mechanisms of PPP2CA in OA pathogenesis, we performed comparative transcriptomic analysis between OA samples with high versus low levels of PPP2CA expression (E-MTAB-4304, GSE114007). Results of GO analysis demonstrated impaired energy homeostasis, showing enrichment in both dAMP catabolism and AMP salvage (a compensatory mechanism activated during cellular energy depletion) (Fig. S4a). These data indicate that *Ppp2ca* deficiency disrupts cellular energy homeostasis, potentially through modulation of AMPK signaling activity. Given the established role of AMPK as a master “energy sensor” that preserves chondrocyte homeostasis by integrating metabolic stress signals, we next sought to determine whether PPP2CA regulates AMPK activity during OA development. To further investigate the mechanism of the PPP2CA function in AMPK signaling during OA, IHC staining revealed increased AMPK- and pAMPK-positive chondrocytes in *Ppp2ca* cKO mice compared to Cre-negative controls (Fig. 3a,b). Real-time PCR analysis of AMPK downstream targets in *Ppp2ca* knockdown ATDC5 cells demonstrated significant upregulation of *Glut4, Pparα, Mtor*, and *Hif1α* mRNA levels following IL-1β-induced injury in ATDC5 cells with *Ppp2ca* knockdown (Fig. 3c-f). Although *Pgc1α* showed no statistically significant difference, its expression trend mirrored those of other AMPK-regulated genes (Fig. 3g). To confirm AMPK signaling as the main downstream which mediating regulatory effects of PPP2CA in OA, chondrocytes were transfected with *Ppp2ca* siRNA and treated with dorsomorphin (an AMPK inhibitor). Consequently, dorsomorphin reversed the protective effects of PPP2CA suppression effectively, evidenced by increased *Mmp3* and *Mmp13* expression (Fig. 3h,i). Dorsomorphin is a multi-target inhibitor that inhibits both AMPK and BMP-2[29,30]. To exclude potential of BMP-2 pathway involvement after PPP2CA inhibition, we treated chondrocytes with the selective BMP-2 inhibitor LDN-193189. While LDN-193189 failed to reverse *Ppp2ca* siRNA-mediated effects, as evidenced by unaltered *Mmp13* expression (Fig. 3k), confirming AMPK signaling as the primary downstream pathway mediating regulatory actions of PPP2CA in OA.

PPP2CA expression level modulates mitochondrial homeostasis in chondrocytes

Transcriptomic analysis between OA samples with high v.s. low-PPP2CA expression revealed significant enrichment of mitochondrial apoptotic pathways alongside compensatory upregulation of mitophagy,

implying higher expression level of PPP2CA mediated mitochondrial dysfunction during OA (Fig. S4a,b). Western blot analysis demonstrated that IL-1β upregulated protein levels of SDHA, UQCRC1, COX4I2, MT-ND4, and ATP5A, while *Ppp2ca* knockdown significantly suppressed these effects (Fig. 4a-i). To investigate the role of the PPP2CA-AMPK signaling pathway in regulating chondrocyte energy metabolism during OA progression, we assessed mitochondrial integrity and reactive oxygen species (ROS) production in ATDC5 cells with *Ppp2ca* knockdown using JC-1 and ROS staining. Following IL-1β-induced injury, *Ppp2ca* knockdown cells exhibited increased mitochondrial aggregates and reduced ROS levels compared to controls (Fig. 4j-m).

Orally administrable YC-LB-100 serve as a drug delivery system to target OA lesions

LB-100 is a selective PPP2CA inhibitor. We used SwissDock[31] technique and performed protein-ligand docking analysis between LB-100 and PPP2CA. LB-100 showed high binding affinity to PPP2CA (Fig, S5a). To develop an orally available drug delivery system with self-driving and self-adaptive capabilities, we developed an engineered biohybrid microrobot system consisting yeast microcapsules (YC) encapsulating LB-100 nanoparticles (YC-LB-100). The working scheme of the YC-LB-100 drug delivery system in an OA animal model showed in Fig. 5a. Briefly, we mixed LB-100 with polyethyleneimine (PEI)-modified nanocarriers to fabricate PEI-LB-100 nanoparticles, which were then loaded into yeast-based biomimetic carriers (YC-LB-100). In animal, YC-LB-100 traverses the intestinal barrier and specifically endocytosed by macrophages in Peyer's patches thereby facilitating its translocation from the intestinal tract into the circulatory. In the circulatory system, macrophages function as endogenous bioengines that leverage their intrinsic inflammatory chemotaxis to actively transport and deliver LB-100 to disease sites (Fig. 5a). PEI-LB-100 showed a crystal morphology under scanning electron microscopy (SEM), confirming successful LB-100 encapsulation (Fig. 5b). Then, we measured the particles size distribution and Zeta potential of PEI-LB-100 (Fig. 5c). Electron microscopy (SEM/TEM) verified proper PEI-LB-100 assembly within YC, evidenced by the development of Janus structure in encapsulated nanoparticles (absent in YC only) (Fig. 5d). High-resolution TEM (HR-TEM) revealed a featureless gray phases contrast lacking lattice fringes, consistent with an amorphous or ultrafine crystalline (< 1 nm) structure (Fig. 5e, left). Energy-dispersive X-ray spectroscopy (EDS) mapping further demonstrated homogeneous nitrogen distribution (purple signal), confirming that nitrogen was atomically dispersed within the amorphous matrix rather than segregated into crystalline nitride (Fig. 5e, right). EDS spectrum showed the element proportion in YC-LB-100 (Fig. 5f). Quantitative analysis revealed that over 75% of LB-100 were successfully encapsulated within YC, coupled with a corresponding drug loading capacity exceeding 30%. (Fig. 5g). We characterized the cumulative release profile of YC-LB-100 across varying pH conditions (Fig. 5h). Within 100 hours, over 15% of LB-100 was released at pH 6.6, while less than 10% cumulative release was observed at pH 7.4. To track nanoparticle distribution after oral administration, we performed *in vivo* fluorescence imaging on animal models. Result showed nanoparticle accumulated at OA lesion areas 1 hour post-administration, peaking at 48 hours (Fig. 5i). The signal intensity progressively declined from 72 to 144 hours, becoming undetectable after 168 hours (Fig. 5i).

Efficacy of PPP2CA Inhibitors delivered by Nano-Yeast Robots in OA treatment

To determine whether PPP2CA inhibition modulates chondrocyte ECM homeostasis, we provided LB-100 (2 μM, 12 h) to IL-1β-stimulated ATDC5 cells (Fig. S5b). We determined the effective concentration range of LB-100 to be 1–5 μM. qPCR analysis demonstrated that LB-100 (2 μM) treatment significantly attenuated IL-1β-induced upregulation of matrix-degrading enzymes *Mmp3* and *Mmp13* (Fig. S5c,d) Importantly, LB-100 restored the expression of key ECM components, significantly increasing *Col2a1* (approximately 1-fold) and *Acan* (approximately 4.5-fold) mRNA levels compared to IL-1β-treated controls (Fig. S5g,h).

To evaluate the analgesic efficacy of PPP2CA inhibition in OA, we performed DMM surgery in 10-week-old C57BL/6 mice and administered YC-LB-100 3-weeks after DMM surgery. Pain sensitivity was assessed through von Frey filament test (mechanical allodynia) and Hot plate test (thermal allodynia). DMM-operated mice exhibited significantly reduced withdrawal thresholds compared to Sham controls, an effect that was markedly attenuated by LB-100 treatment (Fig. 6a). Spontaneous pain behaviours were analyzed using the LABORAS™ system, significantly greater movement trajectories (Fig. 6b), improved locomotion activity (Fig. 6c), increased travel distance (Fig. 6d), increased rearing (Fig. 6f) and climbing activities (Fig. 6g), and reduced immobility time (Fig. 6h) were observed after treatment with LB-100, compared to untreated OA controls.

Micro-CT analysis revealed that treatment with LB-100 significantly reduced both osteophyte formation (Fig. 6i) and subchondral bone volume (Fig. 6j) relative to OA controls. Histological assessment of Safranin O/Fast Green-stained sections using the OARSI scoring system demonstrated that LB-100 treatment reduced cartilage degradation by approximately 65% compared to untreated OA mice (Fig. 6k,l), with partial preservation of cartilage area (Fig. 6m). IHC analysis showed LB-100 significantly decreased expression of catabolic markers ADAMTS5 (Fig. 6n,o), MMP13 (Fig. S6a,b), and CCL2 (Fig. S6a,c), while increasing Aggrecan-positive area in cartilage (Fig. 6n,p). Histopathological examination confirmed no evidence of organ toxicity in liver, heart, kidney, spleen, or lung tissues in the mice receiving LB-100 treatment (Fig. S6d-h).

Discussion

Accumulating evidence indicates that metabolic reprogramming plays a pivotal role in the pathogenesis of OA[32]. We propose that phosphorylation serves as the most critical PTM governing metabolic reprogramming through dynamic regulation of signalling cascades controlling energy utilization and metabolism during OA progression. In our study, we define PPP2CA, a serine/threonine phosphatase, as a key regulator in OA pathogenesis, where it promoted disease progression by impairing AMPK-mediated energy homeostasis. Furthermore, PPP2CA upregulation reduced oxidative phosphorylation capacity and promoted mitochondrial apoptosis, indicating its regulatory role in energy metabolism through the AMPK dephosphorylation-mediated mitochondrial dysfunction. Finally, we evaluated LB-100, a small

molecule of PPP2CA inhibitor with reported therapeutic potential in multiple cancer types[33,34], and demonstrated its ability to attenuate PPP2CA-driven OA progression. Notably, LB-100 emerged as a promising therapeutic candidate for OA treatment, particularly when combined with our designed Nano-Yeast Robot system (YC-LB-100) for targeted drug delivery.

Prior research has link energy metabolism dysregulation to OA pathophysiology. For example, the multi-omics study revealed that dysregulated energy metabolism significantly compromises chondrocyte function during OA development[35]. Meanwhile, numerous studies demonstrate that the phosphorylation-dephosphorylation equilibrium is critical for maintaining articular chondrocyte integrity and function, while its dysregulation (driven by abnormal expression of phosphatases) is mechanistically linked to OA progression[36,37]. Notably, our discovery of aberrant phosphosites in OA cartilage specimens confirms that phosphorylation homeostasis is essential for chondrocyte protection and OA prevention. Nevertheless, investigations into the dysregulation of energy metabolism in OA through the perspective of phosphorylation-dephosphorylation equilibrium are remarkably few to date. Our study of PP2A phosphatase reveals an association between impaired chondrocyte phosphorylation-dephosphorylation dynamics and energy reprogramming during OA development.

Previous studies have identified PP2A as the major phosphatase responsible for dephosphorylating AMPK across various cell types, such as human liver cancer cell (HepG2)[38], rat aortic smooth muscle (A7r5)[39] and human umbilical vein endothelial cells (HUVECs)[40]. Yet, how PP2A functions in diseased chondrocytes remains unclear. Recent studies indicate that the activation of AMPK (by metformin) can suppress OA development[40,41]. Our study demonstrate that PPP2CA, the catalytic subunit of PP2A, accelerates OA by suppressing AMPK signalling, establishing AMPK as primary downstream target of PP2A in OA pathogenesis. AMPK signalling is one of the critical energy-sensing pathways that maintains cellular energy homeostasis[42]. Cumulative research findings demonstrate that AMPK signalling disruption induces mitochondrial dysfunction, characterized by impaired oxidative phosphorylation, reduced ATP biosynthesis, elevated ROS production, and increased mitochondrial apoptosis in multiple cancers, cardiovascular diseases and Alzheimer's diseases[43–45] PPP2CA upregulation in our OA model directly impaired mitochondrial function, associating with reduced oxidative phosphorylation capacity, induced cellular ROS levels, compromised mitochondrial integrity, and ultimately mitochondrial apoptosis. Collectively, our findings establish that PPP2CA dysregulates energy metabolism through AMPK dephosphorylation-dependent mitochondrial impairment.

OA burdens millions worldwide, yet still lacks disease-modifying treatments. While OA pathogenesis involves multifactorial mechanisms, our results demonstrated that aberrant PPP2CA expression drove phosphorylation-dephosphorylation homeostasis disruption, impairing AMPK-mediated energy production, ultimately causing metabolic dysregulation during OA development. These findings implicate PPP2CA as a potential therapeutic target for OA. Notably, LB-100, a selective PPP2CA inhibitor, demonstrates disease-modifying potential for the OA population. Previously, LB-100 was reported as a candidate for treating multiple cancer types. However, phase I clinical trial data (for cancer) revealed

dose-limiting nephrotoxicity (grade 3 reversible increase in serum creatinine) of LB-100 at 3.1 mg/m², highlighting potential safety concerns for therapeutic applications[46]. Here, we designed an orally administrable drug delivery system, YC-LB-100. This drug delivery system exhibits autonomous navigation capabilities, enabling targeted inflammatory sites through enzyme-macrophage switching[47]. Our results reveal that YC-LB-100 achieves targeted accumulation at the OA site and sustains LB-100 release for over 100 hours. Significantly, YC-LB-100 administration reversed pain behaviors and prevented OA progression in mice following DMM surgery. Altogether, YC-LB-100 emerges as a clinically translational candidate that is capable of restoring chondrocyte homeostasis and exhibits the potential of disease-modifying capacity in OA.

In summary, OA progression is driven by PPP2CA-mediated AMPK dephosphorylation, disrupting mitochondrial oxidative phosphorylation and promoting chondrocyte energy metabolic failure. We engineered YC-LB-100, an orally administered yeast-microcapsule system that targets PPP2CA inhibition to inflamed joints via macrophage-mediated transport. YC-LB-100 restored AMPK signalling, reversed pain behaviors, and attenuated cartilage degeneration through sustained LB-100 release (> 100h). Although LB-100 exhibited dose-limiting nephrotoxicity in cancer trials, encapsulation in YC reduced systemic exposure while still maintaining therapeutic efficacy. This work establishes PPP2CA inhibition (LB-100) as a disease-modifying strategy for OA by ameliorating dephosphorylation-dependent energy metabolic dysfunction. The YC-LB-100 delivery system provides novel insights into how bioengineered platforms can repurpose potentially toxic inhibitors for clinically viable OA treatment.

Materials and Methods

Cell Culture

The ATDC5 cell line was maintained in DMEM/F12 (Gibco) supplemented with 10% FBS (Gibco), and 1% Pen-Strep (10,000 units penicillin and 10 mg streptomycin/mL, Sigma-Aldrich) at 37°C under 5% CO_2 with 70–80% humidity. During cell culture, the medium was replaced every 3 days to prevent nutrient depletion. Cells were passaged at 85–90% confluency using Trypsin-EDTA (0.05%, Gibco) for 5 min at 37°C. Enzymatic digestion was terminated by adding an equal volume of complete growth medium. The cell suspension was centrifuged at 300 × g for 5 min, resuspended in fresh growth medium, and seeded into new culture plates.

Protein extraction and western blot analysis

Cells were washed three times with ice-cold PBS and lysed in buffer containing 50 mM Tris-HCl (pH 7.4), 150 mM NaCl, 20 mM EDTA, 1% Triton X-100, 1% sodium deoxycholate, 0.1% SDS, and protease inhibitors (complete details in Table S1). Lysates were incubated on ice for 10 min, followed by centrifugation at 12,000g for 10 min at 4°C to collect supernatants. Protein concentrations were determined using a BCA assay (Thermo Fisher Scientific).

Proteins (20–30 μg per lane) were resolved by 10% SDS-PAGE and transferred to PVDF membranes (Bio-Rad). Membranes were blocked in PBS containing 5% non-fat dry milk and 0.1% Tween-20 for 1 h at room temperature, then incubated overnight at 4°C with primary antibodies (Table S1) diluted in blocking buffer. After washing, membranes were probed with HRP-conjugated secondary antibodies (1:5,000) for 1 h at room temperature. Signals were detected using enhanced chemiluminescence (ECL; Thermo Fisher Scientific) and imaged with a ChemiDoc system (Bio-Rad).

Immunofluorescence

Paraffin-embedded sections were baked at 60°C for 1 h, dewaxed in xylene, and rehydrated through graded ethanol. Antigen retrieval was performed by incubating sections in sodium citrate-EDTA buffer (10 mM sodium citrate, 2 mM EDTA, pH 6.0) at 65°C overnight. After cooling to room temperature, sections were washed three times in PBS (5 min per wash) and encircled with a hydrophobic barrier pen to create defined staining areas.

Sections were permeabilized with 0.5% Triton X-100 in PBS for 10 min. Non-specific binding was blocked with 5% goat serum in PBS for 1 h at 37°C. Primary antibodies (diluted in blocking buffer according to Table S1) were applied and incubated overnight at 4°C.

After thorough washing (3×15 min in PBS), sections were incubated with appropriate Alexa Fluor-conjugated secondary antibodies (1:500 in blocking buffer) for 2 h at room temperature. Nuclear counterstaining was performed by adding DAPI (1 μg/mL in PBS) during the final 15 min of secondary antibody incubation. Following final washes (3×15 min in PBS), slides were mounted with antifade medium and stored at 4°C protected from light.

Images were acquired using a Leica DM2000 LED microscope equipped with LAS X software (v3.7), maintaining consistent exposure settings across compared samples. Fluorescence quantification was performed in ImageJ (NIH) using standardized thresholds, with negative controls (primary antibody omitted) included in each experiment to validate staining specificity. All antibodies were verified using appropriate positive and negative control tissues, with catalog numbers and validation data provided in Supplementary Table 1.

RNA Extraction and Quantitative Real-Time PCR

Total RNA was isolated from ATDC5 cells treated with or without 20 ng/mL IL-1β, 30nM siPPP2CA (Selleck) and 20nM LDN-193189 (Selleck) for 24 h using TRIzol reagent (Invitrogen). Cells were washed three times with ice-cold PBS before adding 1 mL TRIzol, followed by thorough pipetting and vortexing for 1 min. After 5 min of lysis at room temperature, samples were transferred to microcentrifuge tubes, mixed with 200 μL chloroform, and centrifuged at 12,000 × g for 15 min at 4°C. The aqueous phase was combined with an equal volume of isopropanol, incubated for 10 min at room temperature, and centrifuged at 13,000 × g for 10 min at 4°C. The RNA pellet was washed with 75% ethanol, air-dried, and

dissolved in RNase-free water. RNA concentration and purity were verified by spectrophotometry (A260/A280 ratio ≥ 1.8; NanoDrop 2000, Thermo Fisher Scientific).

Reverse transcription was performed using 1 μg total RNA with ReverTra Ace qPCR RT Master Mix (TOYOBO) according to the manufacturer's protocol. qPCR was carried out in triplicate using SYBR Green Master Mix (Applied Biosystems) on a QuantStudio 6 Flex system (Thermo Fisher Scientific). Primer sequences for target genes (Mmp3, Mmp13, Adamts4, Adamts5, Col2a1, Acan, Ccl2, Glut4, Pparα, Mtor, Hif1α, Pgc1α, Sirt1, Foxo1) and the reference gene (b-Actin) are listed in Supplementary Table 2. Relative mRNA levels were calculated by the Ct (2 − ΔΔCT) method, with normalization to b-Actin.

Mass spectrometry

Articular cartilage tissues were collected from osteoarthritis patients undergoing joint replacement surgery, with samples classified as worn or non-worn based on macroscopic evaluation of cartilage degeneration. Proteins were extracted using RIPA buffer supplemented with protease inhibitors, followed by reduction, alkylation, and tryptic digestion. Peptides were desalted using C18 StageTips and labeled with TMT 11-plex reagents (Thermo Scientific) according to the manufacturer's protocol. Phosphopeptides were enriched using TiO2 microspheres (GL Sciences) before liquid chromatography-tandem mass spectrometry (LC-MS/MS) analysis on a Q Exactive HF-X mass spectrometer (Thermo Scientific) coupled to an EASY-nLC 1200 system. Raw data were processed using MaxQuant (v1.6.17.0) and searched against the UniProt human proteome database (release 2021_03) with a false discovery rate (FDR) set to 1% at both peptide and protein levels.

Mouse Model Generation

Chondrocyte-specific *Ppp2ca* knockout mice (*Ppp2ca* cKO) were generated by crossing $Ppp2ca^{f/f}$ mice with Col2-CreER mice. Littermate Cre^{-} mice served as controls. Genotyping was performed by PCR analysis of tail DNA using primers spanning the floxed region (sequences in Supplementary Table X). To induce recombination, 2-week-old *PPP2CA* cKO mice received intraperitoneal tamoxifen (1 mg/10 g body weight; Sigma T5648) dissolved in corn oil for 5 consecutive days. Phenotypic analyses were conducted 3 months post-induction to allow for complete gene deletion and phenotypic manifestation. Control mice received equivalent tamoxifen treatment.

Destabilization of the Medial Meniscus (DMM) Mouse Model

To establish OA, 12-week-old male C57BL/6 mice underwent DMM surgery under isoflurane anesthesia (3% induction, 1.5% maintenance). The surgical site was prepared by hair removal and iodine disinfection, followed by a medial parapatellar incision to expose the knee joint. The medial meniscotibial ligament was transected using micro-scissors under 20× magnification. After saline irrigation, the joint capsule was closed with 6 – 0 absorbable sutures and the skin with 5 – 0 non-absorbable sutures. Postoperative care included subcutaneous buprenorphine (0.1 mg/kg every 12 h for

48 h) for analgesia and intramuscular penicillin (40,000 IU/kg daily for 2 days) for infection prophylaxis. Sham-operated controls received identical procedures without ligament transection.

Beginning 2 weeks post-DMM, mice received weekly intra-articular injections for 4 weeks: experimental groups were administered LB-100 (2 mg/kg in 10 μL saline), positive controls received celecoxib (5 mg/kg in vehicle), and negative controls received saline alone. Pathological analysis was performed after a 1-week washout period. For transgenic studies, *PPP2CA* cKO mice and Cre^- littermates were analysed at 1- and 3-month endpoints following behavioural assessment.

Animal Studies

Sixteen-week-old male C57BL/6 mice (weight range: 25–30 g; GemPharmatech Biotechnology Co., Ltd.) were maintained under specific pathogen-free (SPF) conditions at 22–25°C with a 12-hour light/dark cycle and ad libitum access to food and water. Following a one-week acclimation period, mice were utilized for two distinct experimental paradigms.

For the chondrocyte-specific PP2Aca deficiency study, mice were randomly assigned to four experimental groups ($n \geq 3$ per group): i) Ctrl (Sham operation), ii) PP2A knockout mice receiving Sham operation, iii) wild-type mice undergoing destabilization of the medial meniscus (DMM) surgery, and iv) PP2A knockout mice subjected to DMM surgery. Osteoarthritis was induced via DMM surgery as previously described. Behavioural assessments were performed using the Laboratory Animal Behaviour Observation Registration and Analysis System (LABORAS™, Metris, Netherlands), followed by tissue collection (liver, kidney, heart, spleen, knee joint) for histological evaluation.

In the therapeutic intervention study assessing PP2A inhibitors delivered by Nano-Yeast Robots, mice were randomized into four treatment groups ($n \geq 3$ per group): i) Ctrl (Sham operation), ii) Sham operation with intra-articular vehicle injection, iii) DMM surgery with intra-articular vehicle injection, and iv) DMM surgery with weekly intra-articular LB-100 administration (40mg/20g) for four weeks. The DMM surgical procedure was performed under general anaesthesia by transecting the medial meniscotibial ligament, while Sham controls received capsule incision and closure without ligament disruption. The experimental timeline is illustrated in Fig. S2.

Behavioral and Pain Assessment

Voluntary activity was monitored over a 12-hour period using the LABORAS. Following body weight measurement, mice were individually placed on testing platforms with free access to food and water. Behavioural recording commenced at 20:00 and continued until 08:00 the following day. Parameters assessed included motion trajectory, total locomotion distance, average speed, climbing frequency, and rearing activity.

OA pain progression was evaluated using Von Frey hair and hotplate tests, as previously described. Mechanical allodynia was measured with calibrated Von Frey filaments (North Coast Medical Inc., CA, USA). Mice were acclimatized for 30 min in Plexiglas enclosures with mesh flooring prior to testing. A

series of filaments (0.04–6.0 g) were applied to the mid-plantar hind paw, beginning with 0.4 g stimulation. The 50% paw withdrawal threshold was determined using the "up-and-down" method, with all assessments conducted by blinded observers.

Histological Analysis

At 16 weeks post-DMM surgery, mouse right knee joints were harvested and fixed in 4% paraformaldehyde for 24 hours. For safranin O/fast green staining, samples were decalcified in formic acid solution (1 week), while EDTA solution (4 weeks) was used for specimens destined for immunohistochemistry. Following dehydration, tissues were paraffin-embedded and sectioned sagittally at 5 μm thickness.

Serial sections underwent safranin O/fast green and hematoxylin-eosin (H&E) staining for morphological evaluation. Disease severity was quantified using Osteoarthritis Research Society International (OARSI) scoring criteria, with additional assessment of cartilage area, synovitis score, osteophyte size, and osteophyte maturity. All histological analyses were performed by observers blinded to experimental groups.

Safranin O/Fast Green Staining Protocol

Knee joint sections were baked in a 65°C oven overnight. Sections were then processed through the following sequence: dewaxing in xylene (3 × 7 minutes), graded alcohol rehydration (100%, 100%, 95%, 75%, and 50% alcohol, followed by ddH2O; 4 minutes each), hematoxylin staining (5 minutes), distilled water rinse (2 minutes), Fast Green counterstaining (1–2 minutes), 1% acetic acid differentiation (30 seconds), Safranin O staining (10 minutes), and final dehydration in anhydrous ethanol (5 seconds) before xylene clearing and mounting with optical resin adhesive.

Hematoxylin-eosin staining

After dewaxing, tissue sections then underwent sequential processing: nuclear staining with hematoxylin (3 minutes), distilled water rinses (2 × 1 minute), bluing in 0.25% ammonia water (3 seconds), and additional distilled water washes (3 × 1 minute). Counterstaining was achieved through eosin (5 seconds) following graded ethanol dehydration (50%, 75%, and 95% ethanol; 1 minute each). Final dehydration steps included 95% ethanol (1 minute), absolute ethanol (1 minute), and xylene clearing before mounting with optical resin adhesive.

Micro-CT analysis

Bone defect and osteophyte formation in murine knee joints were assessed using micro-computed tomography (μCT). Following overnight fixation in 4% formaldehyde at 4°C, specimens were rinsed with PBS and scanned using a Venus® μCT system (Pingsheng Healthcare) operated at 90 kV and 65 μA with an isotropic voxel size of 10 μm. Image reconstruction and analysis were performed using Avatar V1.6.6 software with consistent thresholding and normalization across all samples.

Quantitative evaluation focused on two anatomical regions: (1) the tibial metaphysis extending 1 mm distal to the growth plate, and (2) the adjacent 1–2 mm subchondral region. Free-form regions of interest were manually delineated to quantify calcified meniscus and osteophyte volumes. Trabecular microarchitecture was characterized by measuring bone mineral density (BMD), bone volume fraction (BV/TV), trabecular number (Tb.N), thickness (Tb.Th), and separation (Tb.Sp). Cortical bone parameters included density (ctBMD) and thickness (Ct.Th).

Immunohistochemistry

Following antigen retrieval in heated repair solution (95°C, 15 min), knee joint sections underwent sequential pretreatment with endogenous peroxidase blocking buffer (Beyotime; 10 min) and 0.5% Triton X-100 permeabilization (37°C, 15 min). Non-specific binding was blocked with goat serum (30 min, 37°C) prior to overnight incubation with primary antibodies at 4°C (antibody details in Table S1). After three PBST washes, sections were incubated with species-matched secondary antibodies (1 h, room temperature), followed by signal amplification using Vectastain Elite ABC Kit (Vector Labs). Immunoreactivity was visualized with ImmPACT DAB Peroxidase Substrate, and quantitative analysis of staining intensity was performed by measuring integrated optical density (IOD) values using ImageJ software (NIH).

RNA-seq analysis

Public RNA sequencing datasets (accessions: E-MTAB-4304, E-MTAB-7313, PRJNA503001, GSE114007) were obtained from the EMBL-EBI or NCBI GEO repositories. To assess differential *PPP2CA* expression across pairwise dataset comparisons, we conducted differential expression analysis of the two conditions using the DESeq2 R package under the significance threshold of Padj < 0.05 and log2 fold change > 1. All possible pairwise comparisons included: E-MTAB-4304 v.s. E-MTAB-7313; E-MTAB-7313 v.s. PRJNA503001; PRJNA503001 v.s. GSE114007; E-MTAB-4304 v.s. GSE114007; E-MTAB-7313 v.s. GSE114007. The comparison E-MTAB-4304 vs. GSE114007 exhibited the most significant differential *PPP2CA* expression. Subsequently, GO and KEGG pathway analyses were performed on this contrast using the GSEA R package.

Statistics

Data are presented as mean ± standard deviation (SD). Between-group comparisons were performed using two-tailed Student's t-tests for two groups, or one-way ANOVA with Tukey post-hoc test for multiple group comparisons, as appropriate for each experimental design. All statistical analyses were conducted using GraphPad Prism 9.0 software (GraphPad Software). *P < 0.05, **P < 0.01, and ***P < 0.001 were considered as statistically significant difference.

Declarations

Ethics

All animal procedures were approved by the Institutional Animal Care and Use Committee (SIAT-IACUC-20230403-YYS-JSYWZX-LK-A2190-01) and conducted under ARRIVE guidelines. The human study protocol was reviewed and approved by the Institutional Review Board of Nanjing Drum Tower Hospital, Affiliated Hospital of Medical School, Nanjing University (Ethics Approval No. NSFC81991514). All human study procedures were performed in accordance with the IRB's guidelines.

AUTHOR CONTRIBUTIONS

Study design: K.L. and D.C. Study conduct and data collection and analysis: K.L., J.L., G.W., Y-C.H., Z.L.,L.Z., R.D., Q.J. and H.S. Data interpretation: K.L., G.W., Y-C.H., Z.L. Drafting the manuscript: K.L., D.C., and H.P. H.S. takes responsibility for the integrity of the data analysis.

Acknowledgements

This work was supported by the National Natural Science Foundation of China (82302757and 82394445), Shenzhen Science and Technology Program (JCY20240813145204006, SGDX20201103095600002), Shenzhen Development and Reform Program (XMHT20220106001), Shenzhen Key Laboratory of Digital Surgical 3D Printing Project (SYSPG20241211173844006), Guangdong Provincial Engineering Technology Research Center for Clinical Translation and Application of Medical 3D Printing Materials (2023B192).

References

1. Leifer, V. P., Katz, J. N. & Losina, E. The burden of OA-health services and economics. *Osteoarthritis Cartilage* 30, 10–16 (2021).
2. Kolasinski, S. L. *et al.* 2019 American College of Rheumatology/Arthritis Foundation Guideline for the Management of Osteoarthritis of the Hand, Hip, and Knee. *Arthritis Care Res (Hoboken)* 72, 149–162 (2020).
3. Zhuo, Q., Yang, W., Chen, J. & Wang, Y. Metabolic syndrome meets osteoarthritis. *Nat Rev Rheumatol* 8, 729–737 (2012).
4. Zhai, G. Alteration of Metabolic Pathways in Osteoarthritis. *Metabolites* 9 (2019).
5. Yun, H. J. *et al.* AMPK-HIF-1α signaling enhances glucose-derived de novo serine biosynthesis to promote glioblastoma growth. *Journal of Experimental & Clinical Cancer Research* 42, 340 (2023).
6. Jäger, S., Handschin, C., St-Pierre, J. & Spiegelman, B. M. AMP-activated protein kinase (AMPK) action in skeletal muscle via direct phosphorylation of PGC-1alpha. *Proc Natl Acad Sci U S A* 104, 12017–12022 (2007).
7. Narkar, V. A. *et al.* AMPK and PPARdelta agonists are exercise mimetics. *Cell* 134, 405–415 (2008).

8. Ng, T. L. *et al.* The AMPK stress response pathway mediates anoikis resistance through inhibition of mTOR and suppression of protein synthesis. *Cell Death Differ* 19, 501–510 (2011).
9. Zhu, X. *et al.* Feedback regulation between AMPK and HIF-1α contributes to color stability via energy metabolism and mitochondrial efficiency regulation of yak meat. *LWT* 199, 116031 (2024).
10. Rabinovitch, R. C. *et al.* AMPK Maintains Cellular Metabolic Homeostasis through Regulation of Mitochondrial Reactive Oxygen Species. *Cell Rep* 21, 1–9 (2017).
11. Petursson, F. *et al.* Linked decreases in liver kinase B1 and AMP-activated protein kinase activity modulate matrix catabolic responses to biomechanical injury in chondrocytes. *Arthritis Res Ther* 15, R77 (2013).
12. Gouda, N. A., Zhakupova, A., Abdelaal, A. M., Ahmad, F. & Elkamhawy, A. The interplay involving oxidative stress and autophagy: Mechanisms, implications, and therapeutic opportunities. *Experimental and Molecular Pathology* 143, 104989 (2025).
13. Toriola, M. A. *et al.* Genetic depletion of the early autophagy protein ATG13 impairs mitochondrial energy metabolism, augments oxidative stress, induces the polarization of macrophages to the M1 inflammatory mode, and compromises myelin integrity in skeletal muscle. *Inflamm Res* 75, 26 (2026).
14. Wang, J. *et al.* AMPK: implications in osteoarthritis and therapeutic targets. *Am J Transl Res* 12, 7670–7681 (2020).
15. Lotz, M. & Loeser, R. F. Effects of aging on articular cartilage homeostasis. *Bone* 51, 241–248 (2012).
16. Pan, F. *et al.* Metformin for Knee Osteoarthritis in Patients With Overweight or Obesity: A Randomized Clinical Trial. *JAMA* 333, 1804–1812 (2025).
17. Kerk, D., White-Gloria, C., Johnson, J. J. & Moorhead, G. B. Eukaryotic-like Phosphoprotein Phosphatase (PPP) enzyme evolution: interactions with environmental toxins and regulatory proteins. *Biosci Rep* 43 (2023).
18. Olsen, J. V. *et al.* Global, In Vivo, and Site-Specific Phosphorylation Dynamics in Signaling Networks. *Cell* 127, 635–648 (2006).
19. Wlodarchak, N. & Xing, Y. PP2A as a master regulator of the cell cycle. *Crit Rev Biochem Mol Biol* 51, 162–184 (2016).
20. Virshup, D. M. & Shenolikar, S. From promiscuity to precision: protein phosphatases get a makeover. *Mol Cell* 33, 537–545 (2009).
21. McCright, B., Rivers, A. M., Audlin, S. & Virshup, D. M. The B56 family of protein phosphatase 2A (PP2A) regulatory subunits encodes differentiation-induced phosphoproteins that target PP2A to both nucleus and cytoplasm. *J Biol Chem* 271, 22081–22089 (1996).
22. Moreno, C. S. *et al.* WD40 repeat proteins striatin and S/G(2) nuclear autoantigen are members of a novel family of calmodulin-binding proteins that associate with protein phosphatase 2A. *J Biol Chem* 275, 5257–5263 (2000).

23. Ochoa, D. *et al.* The functional landscape of the human phosphoproteome. *Nature Biotechnology* 38, 365–373 (2020).
24. Götz, J., Probst, A., Mistl, C., Nitsch, R. M. & Ehler, E. Distinct role of protein phosphatase 2A subunit Calpha in the regulation of E-cadherin and beta-catenin during development. *Mech Dev* 93, 83–93 (2000).
25. Bhardwaj, A. *et al.* Restoration of PPP2CA expression reverses epithelial-to-mesenchymal transition and suppresses prostate tumour growth and metastasis in an orthotopic mouse model. *Br J Cancer* 110, 2000–2010 (2014).
26. Yoon, S. *et al.* PP2A negatively regulates the hypertrophic response by dephosphorylating HDAC2 S394 in the heart. *Exp Mol Med* 50 (2018).
27. Zhu, L. *et al.* Cerebral endothelial 3-mercaptopyruvate sulfurtransferase improves ischemia-induced cognitive impairment via interacting with protein phosphatase 2A. *Acta Pharm Sin B* 15, 314–330 (2024).
28. Tian, R. *et al.* MSdb: An integrated expression atlas of human musculoskeletal system. *iScience* 26, 106933 (2023).
29. Yu, P. B. *et al.* Dorsomorphin inhibits BMP signals required for embryogenesis and iron metabolism. *Nat Chem Biol* 4, 33–41 (2007).
30. Madsen, J. F. *et al.* Dorsomorphin inhibits AMPK, upregulates Wnt and Foxo genes and promotes the activation of dormant follicles. *Commun Biol* 7, 747 (2024).
31. Goullieux, M., Zoete, V. & Röhrig, U. F. Two-Step Covalent Docking with Attracting Cavities. *Journal of Chemical Information and Modeling* 63, 7847–7859 (2023).
32. Mobasheri, A. *et al.* The role of metabolism in the pathogenesis of osteoarthritis. *Nature Reviews Rheumatology* 13, 302–311 (2017).
33. Hong, C. S. *et al.* LB100, a small molecule inhibitor of PP2A with potent chemo- and radio-sensitizing potential. *Cancer Biol Ther* 16, 821–833 (2015).
34. D'Arcy, B. M. *et al.* The Antitumor Drug LB-100 Is a Catalytic Inhibitor of Protein Phosphatase 2A (PPP2CA) and 5 (PPP5C) Coordinating with the Active-Site Catalytic Metals in PPP5C. *Mol Cancer Ther* 18, 556–566 (2019).
35. Wu, X. *et al.* Dysregulated energy metabolism impairs chondrocyte function in osteoarthritis. *Osteoarthritis Cartilage* 31, 613–626 (2022).
36. Wang, L. *et al.* SHP2 ablation mitigates osteoarthritic cartilage degeneration by promoting chondrocyte anabolism through SOX9. *FASEB J* 38, e70013 (2024).
37. Chen, C. *et al.* Compression regulates gene expression of chondrocytes through HDAC4 nuclear relocation via PP2A-dependent HDAC4 dephosphorylation. *Biochim Biophys Acta* 1863, 1633–1642 (2016).
38. Wang, T. *et al.* PP2A mediated AMPK inhibition promotes HSP70 expression in heat shock response. *PLoS One* 5 (2010).

39. Joseph, B. K. *et al.* Inhibition of AMP Kinase by the Protein Phosphatase 2A Heterotrimer, PP2APpp2r2d. *J Biol Chem* 290, 10588–10598 (2015).
40. Han, W.-M., Hong, Y.-X., Xiao, G.-S., Wang, R.-Y. & Li, G. NMDARs activation regulates endothelial ferroptosis via the PP2A-AMPK-HMGB1 axis. *Cell Death Discov* 10, 34 (2024).
41. Zhu, Z. *et al.* AMPK activator decelerates osteoarthritis development by inhibition of β-catenin signaling in chondrocytes. *J Orthop Translat* 38, 158–166 (2022).
42. Liu-Bryan, R. Inflammation and intracellular metabolism: new targets in OA. *Osteoarthritis Cartilage* 23, 1835–1842 (2015).
43. Wu, S. & Zou, M.-H. AMPK, Mitochondrial Function, and Cardiovascular Disease. *Int J Mol Sci* 21 (2020).
44. D'Alessandro, M. C. B., Kanaan, S., Geller, M., Praticò, D. & Daher, J. P. L. Mitochondrial dysfunction in Alzheimer's disease. *Ageing Res Rev* 107, 102713 (2025).
45. Lee, Y., Itahana, Y., Ong, C. C. & Itahana, K. A redox-dependent mechanism for AMPK dysregulation interrupts metabolic adaptation of cancer under glucose deprivation. *bioRxiv* (2021).
46. Chung, V. *et al.* Safety, Tolerability, and Preliminary Activity of LB-100, an Inhibitor of Protein Phosphatase 2A, in Patients with Relapsed Solid Tumors: An Open-Label, Dose Escalation, First-in-Human, Phase I Trial. *Clin Cancer Res* 23, 3277–3284 (2016).
47. Zhang, B. *et al.* Twin-bioengine self-adaptive micro/nanorobots using enzyme actuation and macrophage relay for gastrointestinal inflammation therapy. *Sci Adv* 9, eadc8978 (2023).

Figures

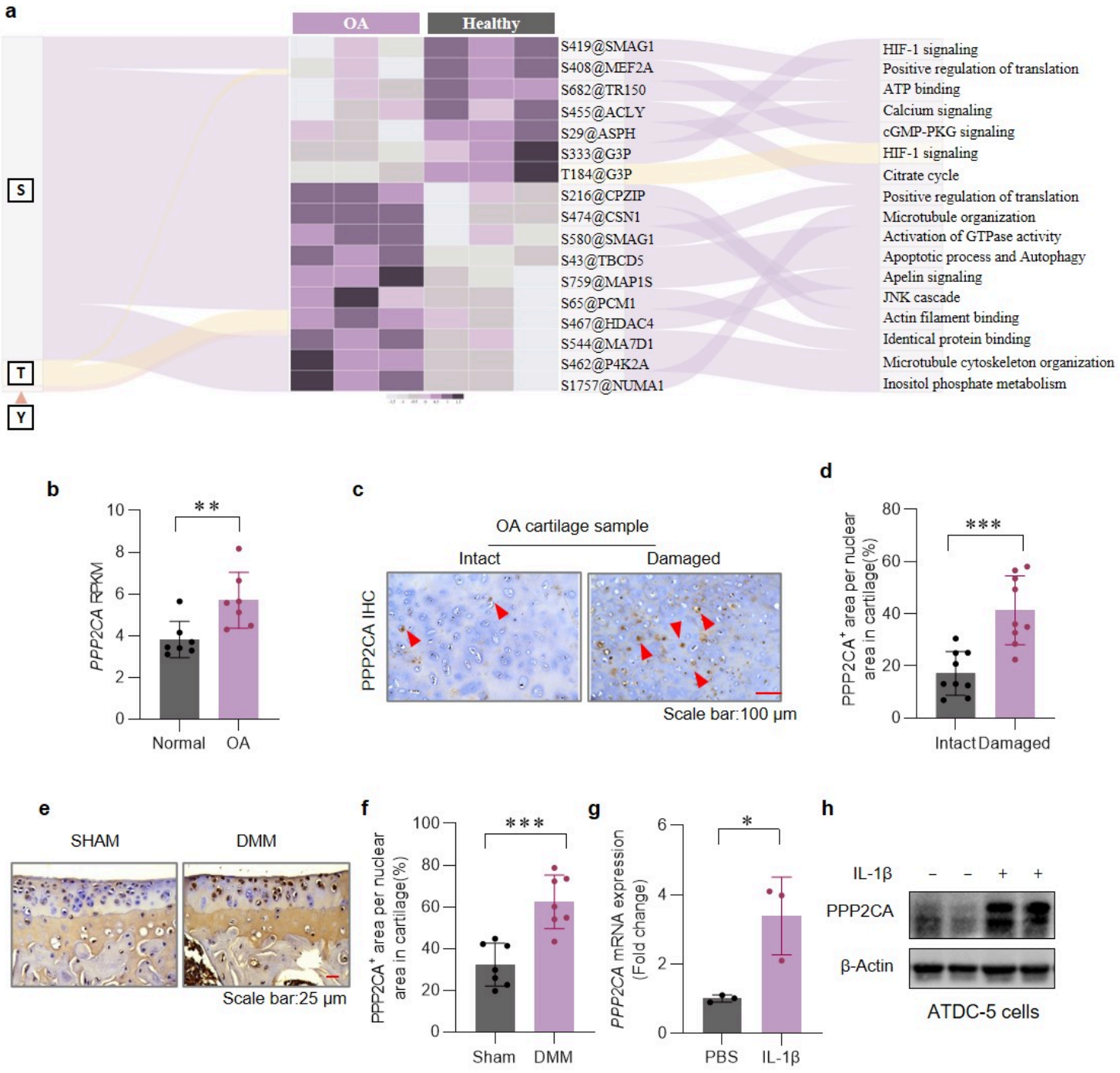


Figure 1

PPP2CA is upregulated during OA progression. (a) Phosphoproteomic profiling identified metabolic reprogramming in OA cartilage through altered phosphorylation patterns. (b) Transcriptomic analysis demonstrated elevated *PPP2CA* mRNA expression in lesioned versus intact cartilage from OA patients. (c-d) Immunohistochemical staining revealed increased PPP2CA protein levels in damaged regions of human OA cartilage compared to preserved areas. (e-f) Consistent with human data, PPP2CA expression was significantly higher in DMM-induced OA mouse joints relative to sham controls by immunohistochemistry. (g) *PPP2CA* transcript levels were upregulated in IL-1β-stimulated ATDC5

chondrocytes versus untreated cells (qRT-PCR). (h) Western blot analysis confirmed increased PPP2CA protein expression following IL-1β treatment. Data represent mean ± SD and analyzed by by two-tailed Student's *t*-test (b,d,f,g). **P* < 0.05, ***P*< 0.01, ****P* < 0.001 were considered as statistically significant; N.S., not significant.

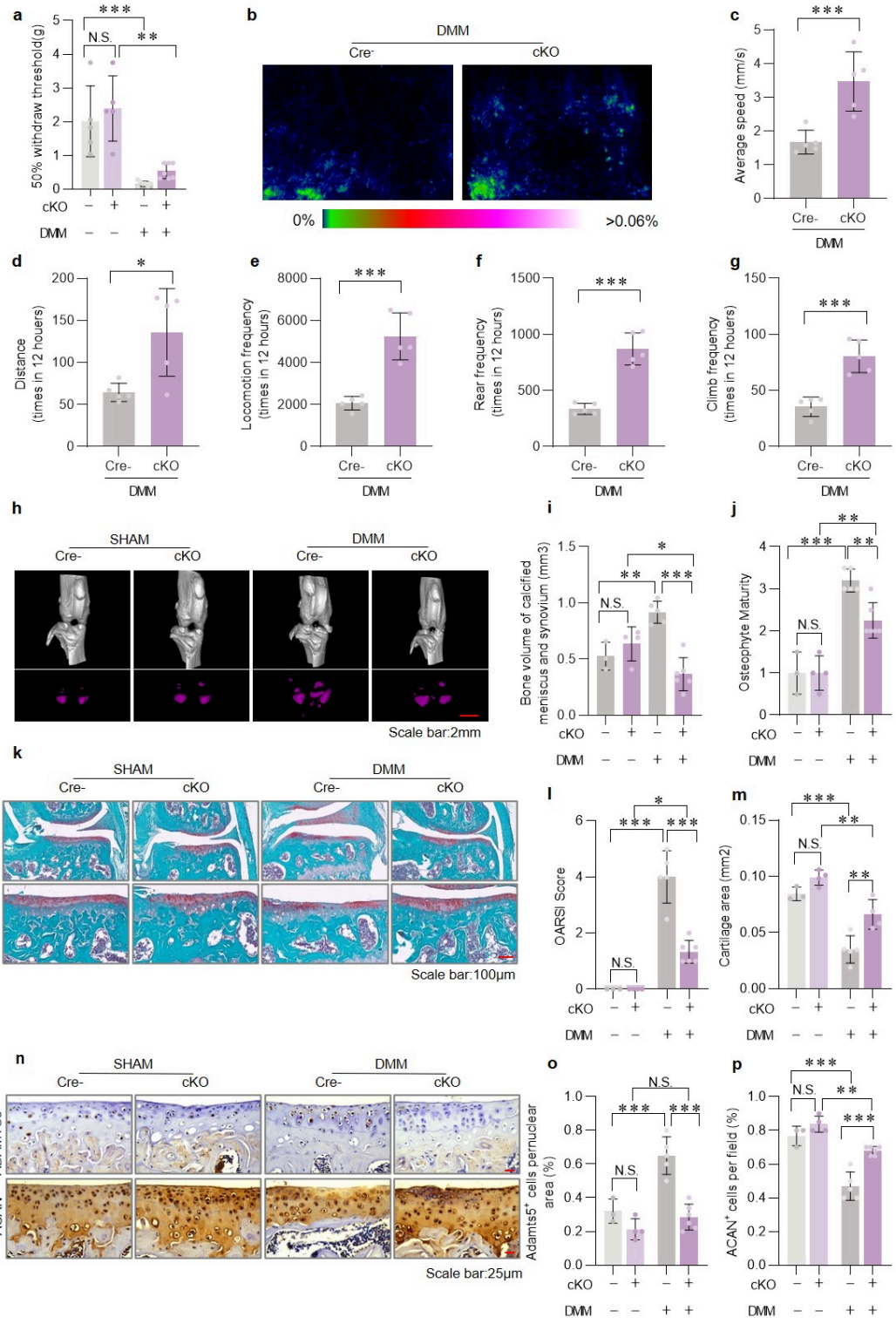


Figure 2

PPP2CA deficiency attenuates osteoarthritis progression in DMM-induced OA mouse model. (a) Mechanical pain sensitivity assessed by von Frey filament test in control (Cre-) and *Ppp2ca* cKO mice following DMM surgery (n≥3). (b-g) LABORAS behavioral analyses showing (b) representative movement trajectories, (c) average velocity, (d) total distance traveled, (e) locomotion frequency, (f) rearing events, and (g) climbing frequency (n≥3). (h-j) Micro-CT evaluation of OA pathogenesis: (h) representative 3D reconstructions (scale bar: 2 mm), (i) osteochondral bone volume, and (j) osteophyte maturity scores (n≥3). (k-m) Histological assessment: (k) Safranin O/Fast Green-stained sections (scale bar: 100 μm), (l) OARSI scores, and (m) cartilage area quantification (n≥3). (n-q) Immunohistochemical analysis of (n) IHC sections (scale bar: 25 μm) showing (o) ADAMTS5^{+} cells, (p) ACAN^{+} cell in articular cartilage (n≥3). Data represent mean ± SD; *P < 0.05, **P < 0.01, ***P < 0.001 by two-tailed Student's *t*-test (c-g) or one-way ANOVA followed by the Tukey post-hoc test (a,i,j,l,m,o,p) were considered as statistically significant; N.S., not significant.

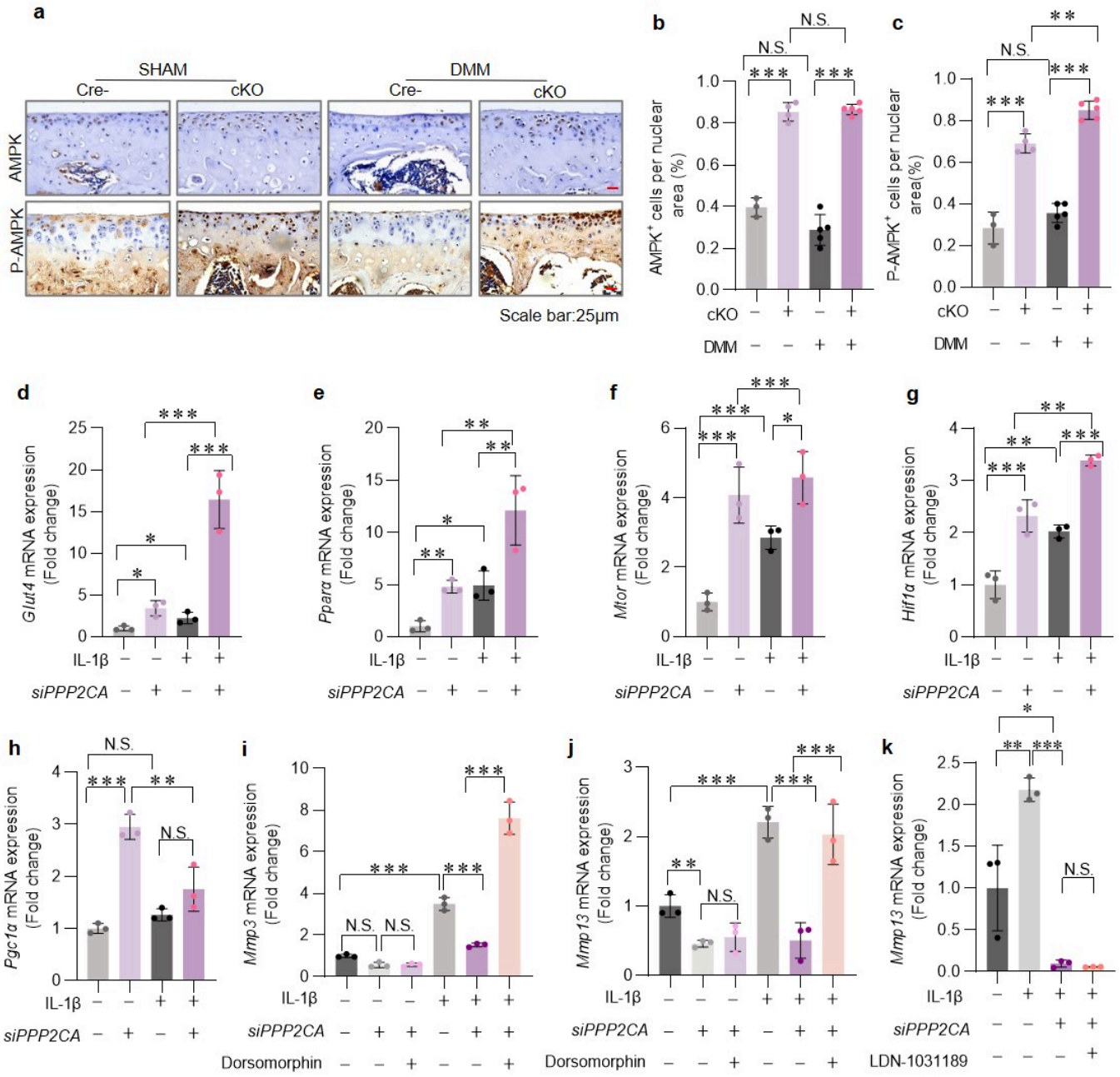


Figure 3

Chondrocyte-specific *Ppp2ca* deficiency activates AMPK signalling pathway. (a-c) Immunohistochemical analysis of AMPK pathway activation in articular cartilage: (a) Representative images (scale bar: 25 μm) with quantification of (b) AMPK+ and (c) p-AMPK+ chondrocytes in Sham or DMM-operated control (Cre^-) and *Ppp2ca* cKO mice (n≥3). (d-h) qPCR analysis of AMPK downstream targets in PPP2CA-knockdown ATDC5 cells: (d) *Glut4*, (e) *Pparα*, (f) *Mtor*, (g) *Hif1α*, and (h) *Pgc1α* mRNA expression (n=3 biological replicates). (i-j) qPCR analysis of (i) *Mmp3* and (j) *Mmp13* expression in IL-1β-treated ATDC5 cells following PPP2CA inhibition and dorsomorphin treatment (n=3 biological replicates). (k) *Mmp13* expression in IL-1b-treated ATDC5 cells following *siPPP2CA* inhibition and LDN-193189 treatment (n=3 biological replicates). Statistical analysis was performed by by two-tailed Student's *t*-test (b) or by three-way ANOVA followed by the Tukey post-hoc test (d-i, k, m); **P* < 0.05, ***P* < 0.01, ****P* < 0.001 were considered as statistically significant, N.S., not significant.

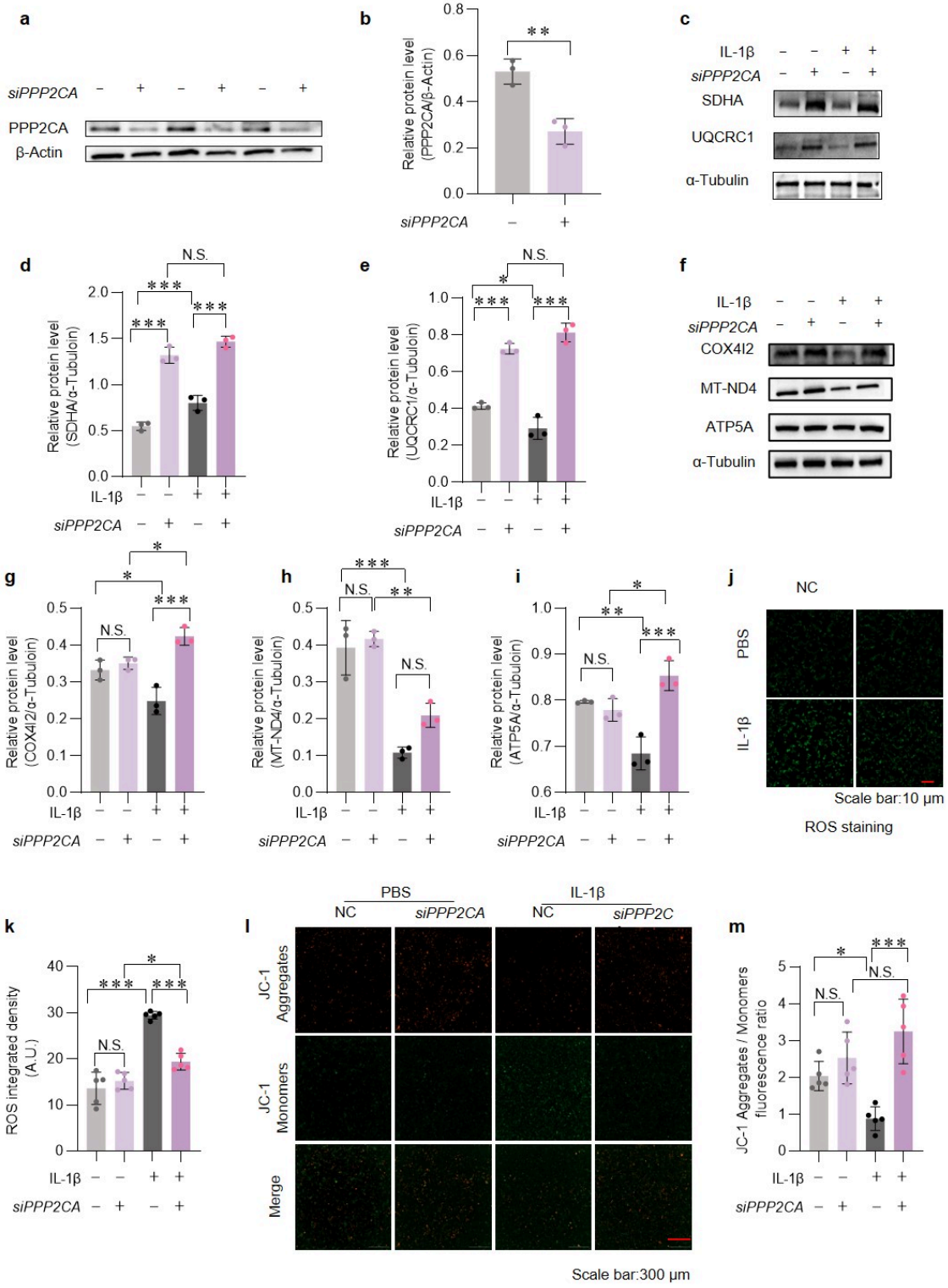


Figure 4

PPP2CA inhibition attenuates mitochondrial dysfunction in chondrocytes.

Western blots and (b) quantification of PPP2CA protein levels in ATDC5 cells (n=3). (c) Western blots and (d-i) quantification of mitochondrial proteins: (d) SDHA, (e) UQCRC1, (f) COX4I2, (g) MT-ND4, and (h) ATP5A (n=3). (j-k) ROS fluorescence staining showing (j) images and (k) quantification of ROS level in IL-

1β-treated ATDC5 cells with or without PPP2CA knockdown. (l-m) JC-1 staining assessing mitochondrial membrane potential: (l) images and (m) monomer/multimer ratio quantification (n=3). Data represent mean ± SD. Statistical analysis was performed by two-way ANOVA followed by the Tukey post-hoc test ; *P < 0.05, **P< 0.01, ***P < 0.001 were considered as statistically significant, N.S., not significant.

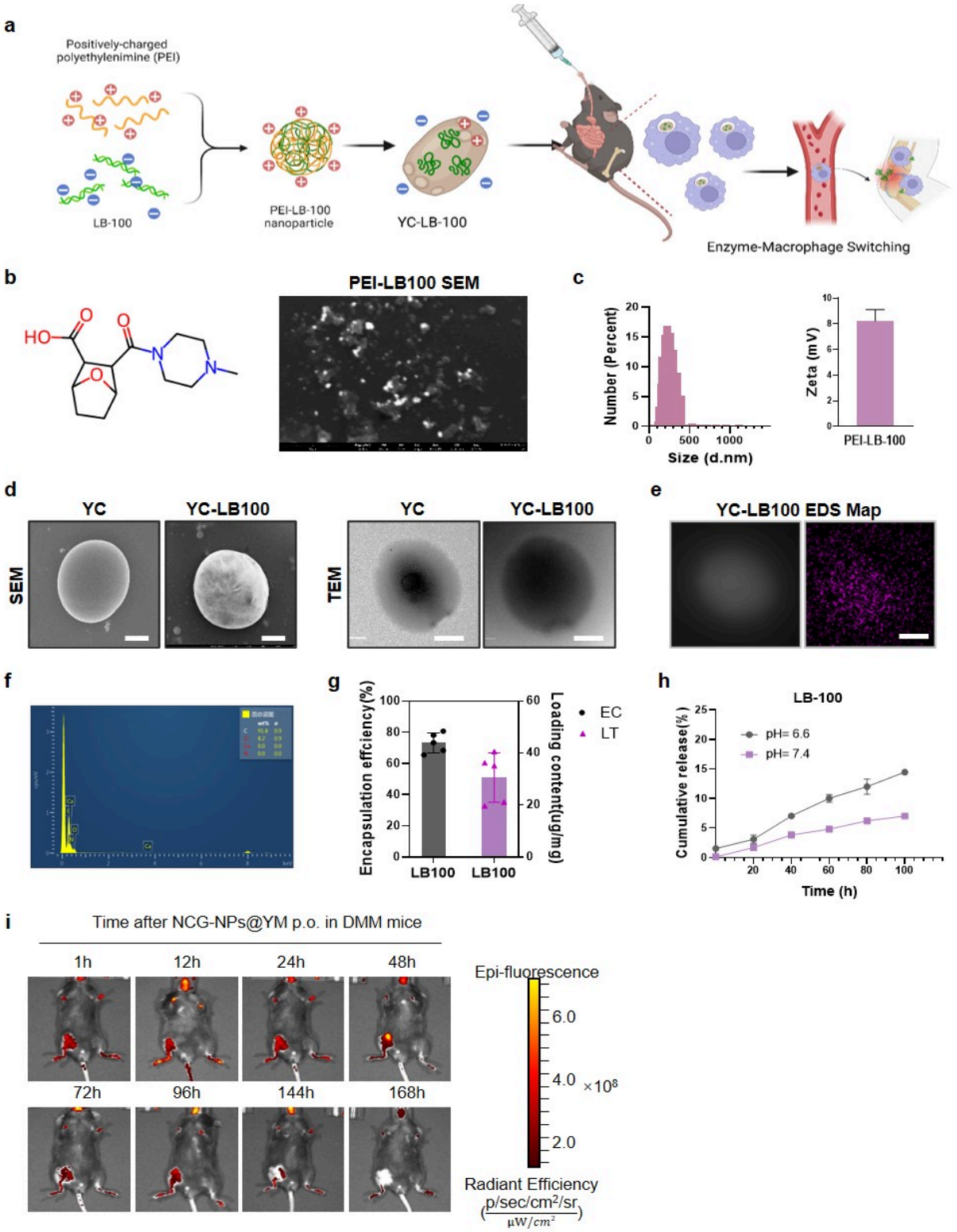


Figure 5

Fabrication and characterization of YC-LB-100 microrobots. (a) Schematic illustration of YC-LB100 preparation and its oral targeted delivery mechanism in an osteoarthritis model. (b) Molecular structure of LB-100 and scanning electron microscopy (SEM) image of PEI-LB100 nanoparticles. Scale bar= 10 mm. (c) Size distribution and zeta potential measurements of PEI-LB100 nanoparticles. (d) Representative SEM and transmission electron microscopy (TEM) images of YC-LB100. Scale bar= 1 mm. (e) HR-TEM image of YC-LB100 and corresponding Energy-dispersive X-ray spectroscopy (EDS) mapping of N in purple. Scale bar= 2.5 mm. (f) EDS spectrum and the element (%) of YC-LB100. (g) Quantitative analysis of encapsulation efficiency and drug loading of YC-LB100.(h) In vitro drug release profile of YC-LB100 under different pH conditions. (i) In vivo fluorescence imaging tracking NCG-NPs following oral administration.

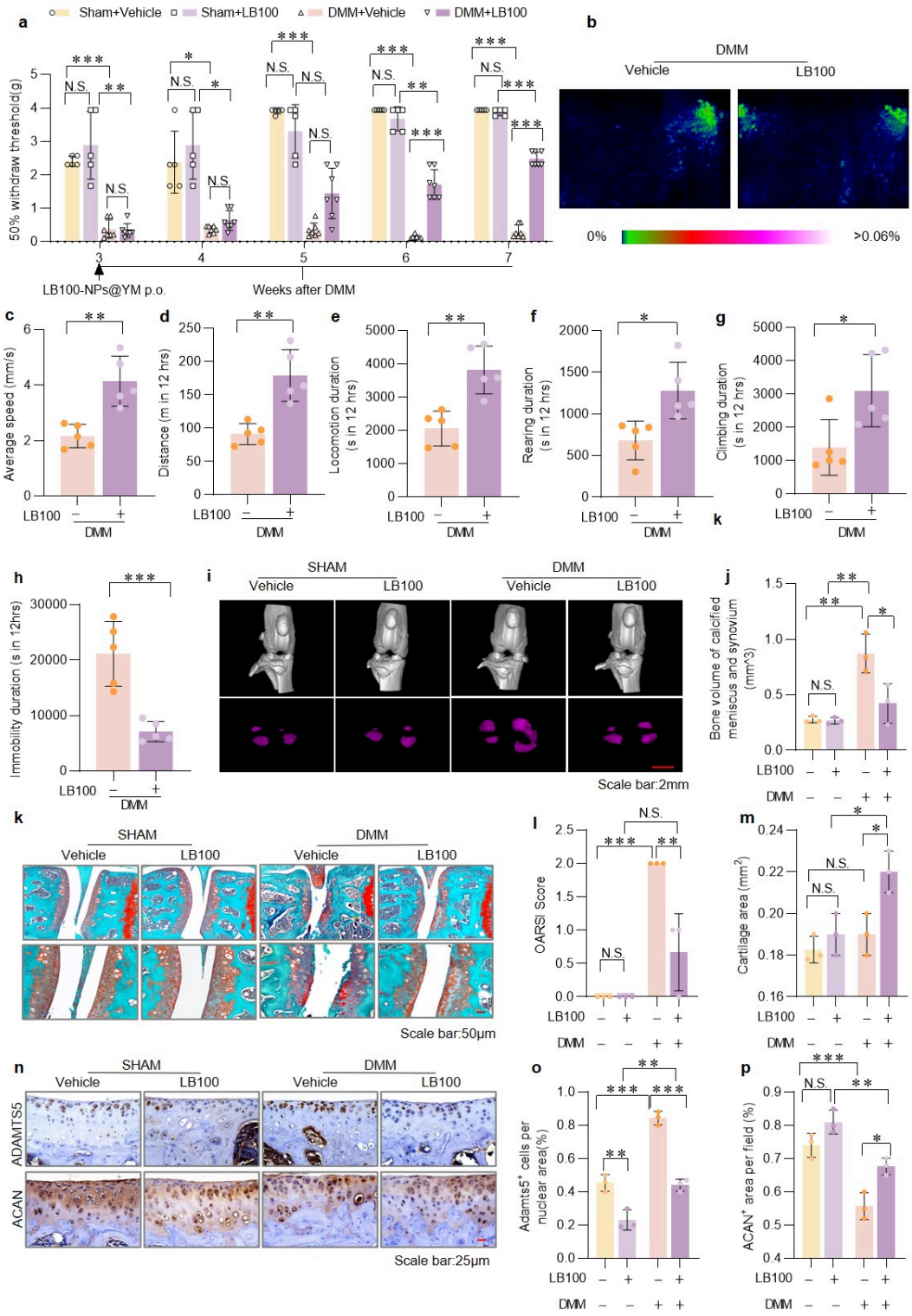


Figure 6

Therapeutic efficacy of YC-LB-100 delivery system in OA model.

Mechanical allodynia assessed by von Frey filament testing in wild-type (WT) and DMM-operated mice treated with vehicle or YC-LB-100. (b) Representative movement trajectories and quantitative analysis of (c) average velocity, (d) total distance travelled, (e) locomotion duration, (f) rearing events, (g) climbing

duration, and (h) immobility time (n≥3). (i-j) Micro-CT evaluation: (i) representative 3D reconstructions (scale bar: 2 mm) and (j) osteochondral bone volume quantification (n≥3). (k-m) Histological assessment: (k) Safranin O/Fast Green-stained sections (scale bar: 50 μm), (l) OARSI scores, and (m) cartilage area (n≥3). (n-p) Immunohistochemical analysis: (n) representative sections (scale bar: 25 μm) showing (o) ADAMTS5+ cells and (p) ACAN+ matrix area (n≥3). Data represent mean ± SD. Statistical analysis was performed by one-way ANOVA followed by the Tukey post-hoc test ; *P < 0.05, **P < 0.01, ***P< 0.001 were considered as statistically significant, N.S., not significant.

Supplementary Files

This is a list of supplementary files associated with this preprint. Click to download.

- Table.docx
- Supplementary.docx